Supplementary Material: Quantum Anomalous Hall Effects Controlled by Chiral Domain Walls

Qirui Cui[1, 2], Jinghua Liang[2], Yingmei Zhu[2], Xiong Yao[2], Hongxin Yang[1, 2, *]

[1] *National Laboratory of Solid State Microstructures, School of Physics, Collaborative Innovation Center of Advanced Microstructures, Nanjing University, Nanjing 210093, China*

[2] *Ningbo Institute of Materials Technology and Engineering, Chinese Academy of Sciences, Ningbo 315201, China*

*Corresponding author: hongxin.yang@nju.edu.cn

Content

Computational Details:

First-Principles Calculations: All first-principles calculations are performed in the Vienna *Ab initio* Simulation Package (VASP) package within the framework of density functional theory (DFT)[1-3]. The exchange-correlation functionals are treated by the generalized gradient approximation (GGA) in the form of Perdew-Burke-Ernzerhof (PBE) functional[4, 5]. The cutoff energies are set to 420 eV, and all structures are fully relaxed until Hellmann-Feynman force of each atom is less than 0.001 eV/Å. Γ-centered $24 \times 24 \times 1$ $\boldsymbol{k}$-point grids are used in calculations to sample the Brillouin zone. The thickness of vacuum area of the two-dimensional materials is more than 15 Å to avoid interactions between periodic slabs. The strong correlation of $3d$ electrons is described by the GGA+U method where U_{eff} is chose to be 3 eV for V[6] and 2.5 eV for Fe[7, 8]. Other U_{eff} ranging from 2 eV to 4 eV are also tested. The key findings that the coexistence of chiral domain wall and quantum anomalous Hall effect in studied systems are robust to the tested U_{eff}. We obtain the maximally localized Wannier functions (MLWFs) from first-principles electronic states by the WANNIER90 package[9]. Here, the MLWFs are further used for calculating Berry curvature, anomalous Hall conductivity, and edge states. Berry curvature is obtained by:

$$\Omega(\boldsymbol{k}) = -\sum_n \sum_{n' \neq n} f_n 2\mathrm{Im} \frac{\langle \psi_{nk}|v_x|\psi_{n'k}\rangle \langle \psi_{n'k}|v_y|\psi_{nk}\rangle}{(E_{n'}-E_n)^2},$$

where f_n refers to the Fermi-Dirac distribution function, $v_{x(y)}$ represents the velocity operator and E_n is the eigenvalue of Bloch wave function ψ_{nk}. Anomalous Hall conductivity is obtained by summarizing the Berry curvature over the Brillouin zone:

$$\sigma_{xy} = \frac{e^2}{h} \frac{1}{2\pi} \int_{BZ} d\boldsymbol{k}^2 \Omega(\boldsymbol{k}).$$

Edge states are obtained by iterative Green function methods, which is implemented in WannierTools package[10].

Phonon Calculations: Phonon spectrums are calculated by the finite displacement method. Real-space force constants are computed using the VASP code with a $4 \times 4 \times 1$ supercell. The convergence tolerance of the force used for phonon calculations is set to 10^{-8} eV/Å. The force-constant matrices and phonon dispersions are calculated using the PHONOPY code[11].

Elastic constant: Elastic constants of VSe_2 and Fe_2XI monolayers are calculated by fitting the formula $E_s = \frac{1}{2}C_{11}\varepsilon_x^2 + \frac{1}{2}C_{22}\varepsilon_y^2 + C_{12}\varepsilon_x\varepsilon_y + 2C_{66}\varepsilon_{xy}^2$ with different external strain. The amplitude of strain ranges from -2% to 2%. For VSe_2 monolayer, $C_{11} = C_{22} = 49.96$ N/m, $C_{12} = 8.61$ N/m, and $C_{66} = 3.58$ N/m. For $Fe_2Cl(Br)I$ monolayer, $C_{11} = C_{22} = 68.83$ (63.84) N/m, $C_{12} = 25.52$ (19.00) N/m, and $C_{66} = 27.11$ (21.70) N/m. The criteria that $C_{11}C_{22} - C_{12}^2 > 0$ and $C_{66} > 0$ is satisfied for both VSe_2 and Fe_2XI monolayers, confirming the mechanical stability.

Calculations of J, K, and $d_\parallel$: (**i**) Three types of magnetic order for a 2×2×1 supercell, FM, G-type AFM, and Stripe-type AFM, are considered. The total energy of these spin configurations can be written as: $E_{FM} = -8J_1 - 8J_2 + E_{other}$, $E_{G-AFM} = 8J_1 - 8J_2 + E_{other}$, and $E_{S-AFM} = 8J_2 + E_{other}$. Accordingly, the nearest-neighboring exchange coupling J_1 and next-nearest-neighboring exchange coupling J_2 can be written as: $J_1 = \frac{E_{G-AFM}-E_{FM}}{16}$, and $J_2 = \frac{2E_{S-AFM}-E_{G-AFM}-E_{FM}}{32}$. (**ii**) The magnetic anisotropy A is defined as the self-consistent energy difference of unit cell with magnetization along positive direction of x axis and z axis. (**iii**) The chirality-dependent energy difference approach is employed for extracting Dzyaloshinskii–Moriya interaction[12]. For VSe_2, a 4×1×1 (1×4×1) supercell with 6×24×1 (24×6×1) k-point mesh is adopted to obtain $d_\parallel^x$ ($d_\parallel^y$). We calculate the self-consistent energies of supercell with clockwise {(0, 0, S); (S, 0, 0); (0, 0, -S); (-S, 0, 0)} and anticlockwise {(0, 0, S); (-S, 0, 0); (0, 0, -S); (S, 0, 0)} spin configurations, and $d_\parallel^x$ or $d_\parallel^y$ equals $(E_{ACW} - E_{CW})/8$. For Fe_2XI (X=Cl, Br), a 2×1×1 supercell with 12×24×1 k-point mesh is adopted to obtain the in-plane component of nearest-neighboring DMI $d_\parallel$. We also calculate the self-consistent energies of the supercell with clockwise {(0, 0, S); (S, 0, 0); (0, 0, -S); (-S, 0, 0)} and anticlockwise {(0, 0, S); (-S, 0, 0); (0, 0, -S); (S, 0, 0)} spin configurations, and $d_\parallel$ equals $(E_{ACW} - E_{CW})/8\sqrt{2}$. To obtain $d_\parallel^{Cl}$, a 4×1×1 supercell with 6×24×1 k-point mesh is adopted. Along the positive direction of x axis, the spin configuration of Fe atoms connected by Cl atoms is set to be clockwise {(0, 0, S); (S, 0, 0); (0, 0, -S); (-S, 0, 0)} or anticlockwise {(0, 0, S); (-S, 0, 0); (0, 0, -S); (S, 0, 0)} while the spin vectors for Fe atoms connected by I atoms are set to be along y direction. We thus obtain that

$d_{\parallel}^{Cl}$ equals $(E_{ACW} - E_{CW})/8$. $d_{\parallel}^{Br}$ could be obtained by the same approach. Moreover, by switching the spin configurations setting between Fe atoms connected by Cl and I atoms, $d_{\parallel}^{I}$ is obtained by the same formula as $d_{\parallel}^{Cl}$. We note that spin-orbit coupling (SOC) effects are neglected in calculations of exchange coupling but considered in calculations of magnetic anisotropy and Dzyaloshinskii–Moriya interaction.

Atomic Spin Model Simulations: To reveal the morphology and dynamics of real-space spin configurations, we numerically solve the stochastic Landau-Lifshitz-Gilbert equations at the atomic level[13]. The gyromagnetic ratio γ is set to 1.76×10^{11} T^{-1}s^{-1}, and the damping constant λ is set to 0.2. The effective magnetic field is only determined by the spin Hamiltonian where the magnetic parameters are obtained from the first-principles calculations. The temperature dependent spin behavior is calculated using the Monte Carlo Metropolis method. In all Monte Carlo simulations, the temperature is gradually increase from 0 to 1000 K with 10 K intervals. For guaranteeing the system reaches thermal stability, 1×10^6 Monte Carlo steps are employed for each temperature point. The open boundary condition is applied in all atomic spin model simulations.

Table SI. The optimized lattice constant (a), magnetic moments of V (m), the NN and NNN exchange coupling (J_1 and J_2), magnetic anisotropy (A), and DMI between the NN V pair ($d_{\parallel}^{x}$ and $d_{\parallel}^{y}$) for VSe$_2$ monolayer. The unit of a is Å; the unit of m is μ_B; the unit of J is meV, the unit of A is meV/atom, and the unit of d is meV. We adopt the sign convention that $J > 0$ ($J < 0$) indicates the ferromagnetic (antiferromagnetic) coupling, $A > 0$ ($A < 0$) indicates out-of-plane (in-plane) magnetic anisotropy, in-plane component of DMI $d > 0$ ($d < 0$) favors clockwise (anticlockwise) spin rotation.

	A	m	J_1	J_2	A	$d_{\parallel}^{x}$	$d_{\parallel}^{y}$
VSe$_2$	3.82	2.00	39.44	-1.12	0.47	2.24	-2.24

Table SII. The optimized lattice constant (a), magnetic moments of Fe (m), the NN and NNN exchange coupling (J_1 and J_2), magnetic anisotropy (A), and DMI between the NN Fe pair ($d_\parallel$) and NNN Fe pair ($d_\parallel^{Cl/Br}$ and $d_\parallel^{I}$) for Fe$_2$XI monolayers. The units and sign convection are given in the caption of Table SI.

	a	m	J_1	J_2	A	$d_\parallel$	$d_\parallel^{Cl}$	$d_\parallel^{Br}$	$d_\parallel^{I}$
Fe$_2$ClI	3.71	3.00	62.74	41.41	0.04	1.17	0.42	-	2.79
Fe$_2$BrI	3.76	3.00	58.98	38.38	0.33	0.67	-	-0.07	1.98
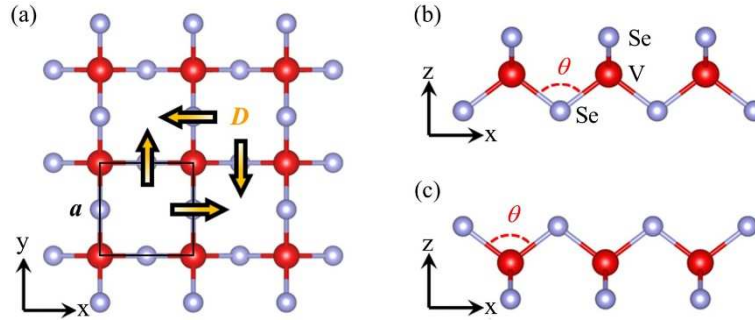
Fig. S1. (a) Top and (b, c) side views of crystal structures of VSe$_2$ monolayer. $P\bar{4}m2$ symmetry guarantees the anisotropic DMI in VSe$_2$ monolayer as indicated by orange arrows.
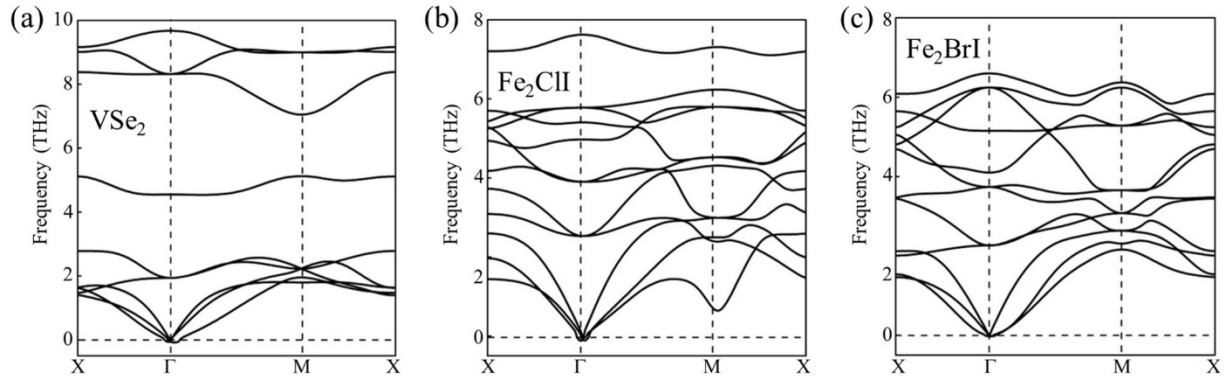

Fig. S2. Phonon dispersions of VSe$_2$, Fe$_2$ClI, and Fe$_2$BrI. Despite there is little acoustic imaginary mode nearby Γ point for Fe$_2$ClI, this instability may not significantly affect the whole crystal structure and can be removed by ripples in structures.
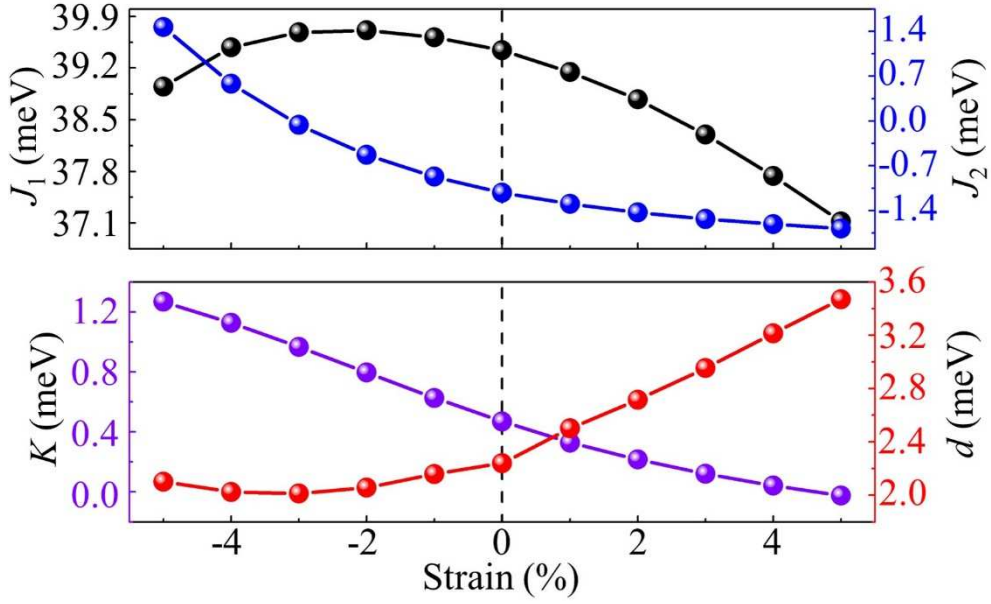
Fig. S3. Strain-dependent magnetic parameters of VSe$_2$. By applying a small tensile strain, the magnitudes of both ferromagnetic exchange coupling and perpendicular magnetic anisotropy that favor the formation of collinear spin configuration obviously decrease while the magnitude of DMI that favor the formation of noncollinear spin configuration increases.
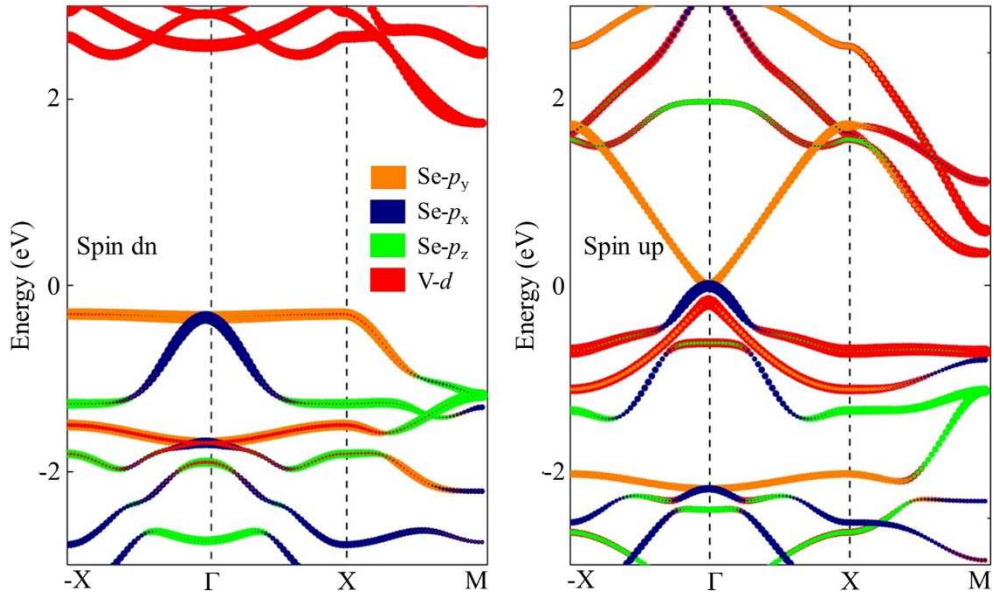

Fig. S4. Orbital resolved spin-down and spin-up band structures of VSe$_2$. One can see that the electronic states nearby the Fermi level are dominated by p_x and p_y orbitals of Se atom.
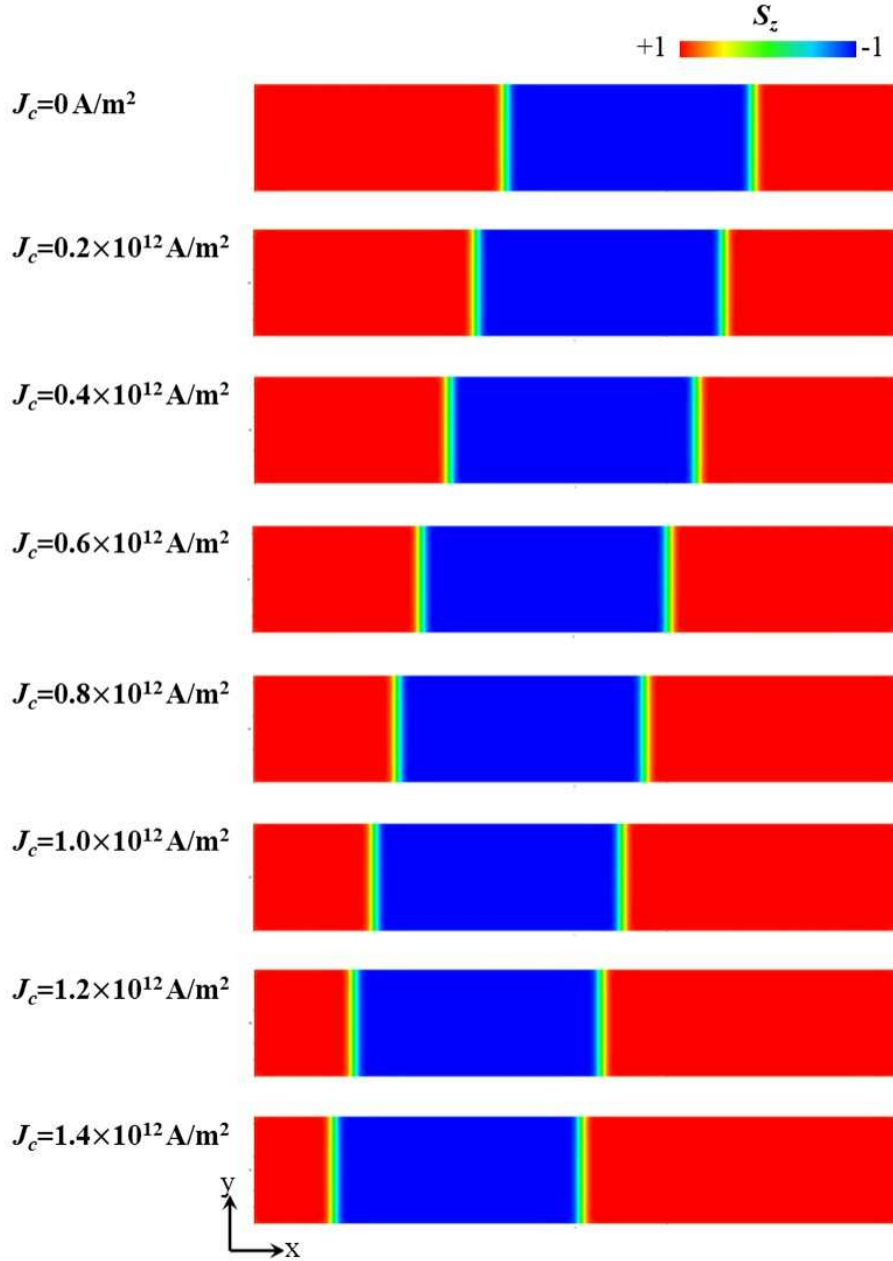
Fig. S5. The top view of relaxed spin configurations of 300×50 nm VSe$_2$ stripe at the time stage $t = 0.1$ ns under the different time-invariant current densities ranging from 0 to 1.4×10^{12} A/m^2. The initial spin configurations, chiral domain wall [see upper panel of Fig. 5(a) in main text], is set to be identical in all simulations. Obviously, larger motion velocity is achieved by injecting stronger spin current.
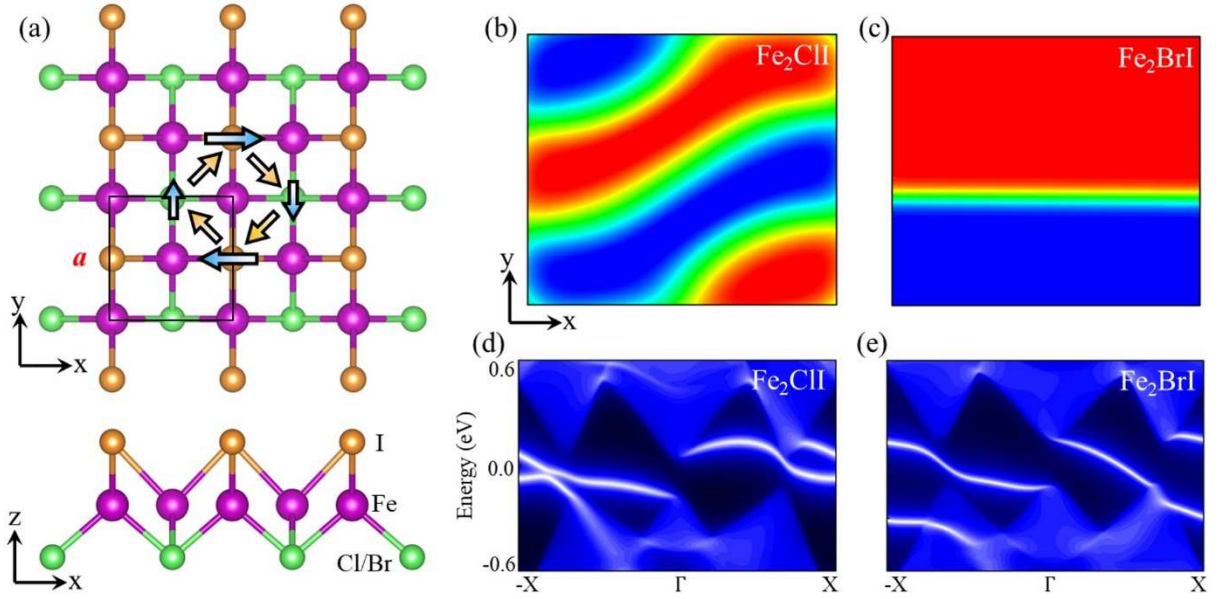
Fig. S6. Coexistence of chiral domain wall and high-Chern-number quantum anomalous Hall effects in Fe_2XI ($X=$ Cl, Br) Janus structures. (a) Top and side views of the crystal structures of Fe_2XI. The inversion symmetry breaking allows the DMI. The arrows in (a) represents the DMI between the first, second, and third neighboring Fe atoms. (b, c) and (d, e) spin configurations and topological edge states of Fe_2ClI and Fe_2BrI monolayers. The zone of simulated spin configuration is set to be a 150 nm×150 nm square.
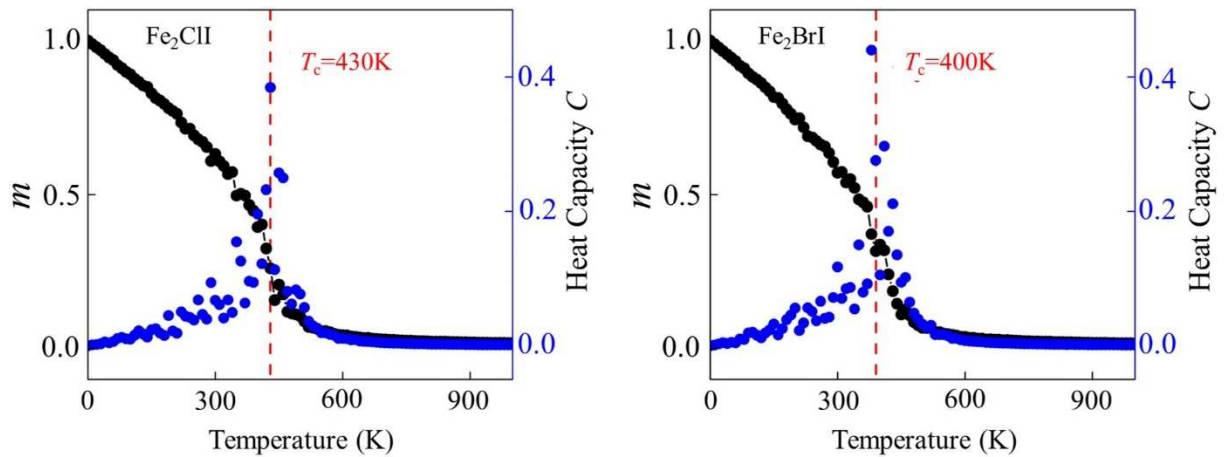

Fig. S7. Temperature-dependent normalized magnetization and heat capacity of Fe_2ClI and Fe_2BrI. The Curie temperature of Fe_2ClI and Fe_2BrI reaches to 430 K and 400 K respectively. The Curie temperature of Fe_2ClI is slightly higher than that of Fe_2BrI due to stronger ferromagnetic exchange coupling.
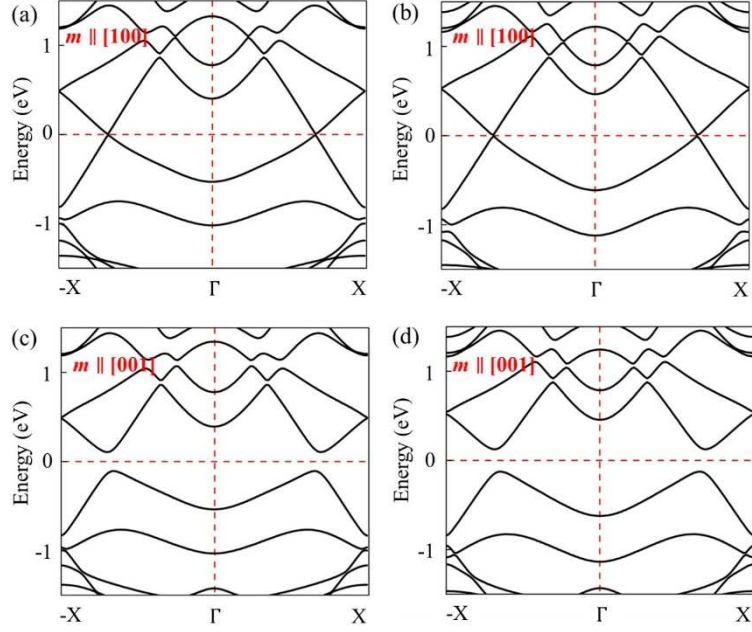
Fig. S8. Magnetization orientation-dependent band structures for Fe_2ClI with magnetization along (a) [100] and (b) [001], and for Fe_2BrI with magnetization along (c) [100] and (d) [001]. Similar to VSe_2, the SOC-induced band gap emerges when the magnetization is perpendicular to the material plane and vanishes when magnetization is in-plane.

Reference:

[1] Kresse G and Hafner J 1993 Phys. Rev. B 47 558-561.
[2] Kresse G and Furthmuller J 1996 Phys. Rev. B 54 11169-11186.
[3] Kresse G and Furthmuller J 1996 J. Comput. Mater. Sci. 6 15-50.
[4] Wang Y and Perdew J P 1991 Phys. Rev. B 44 13298-13307.
[5] Kresse G and Joubert D 1999 Phys. Rev. B, 59 1758-1775.
[6] Cui Q, Zhu Y, Ga Y, Liang J, Li P, Yu D, Cui P and Yang H X 2022 Nano Lett. 22 2334-2341.
[7] Heyd J, Scuseria G E and Ernzerhof M 2003 J. Chem. Phys. 118 8207.
[8] Guo S-D, Mu W-Q, Xiao X-B and Liu B-G 2021 Nanoscale 13 12956-12965.
[9] Mostofi A A, Yates J R, Lee Y-S, Souza I, Vanderbilt D and Marzari N 2008 Comput. Phys. Commun. 178 685.
[10] Wu Q S, Zhang S N, Song H-F, Troyer M and Soluyanov A A 2018 Comput. Phys. Commun. 224 405.
[11] Togo A and Tanaka I 2015 Scr. Mater. 108 1-5.
[12] Yang H, Thiaville A, Rohart S, Fert A and Chshiev M 2015 Phys. Rev. Lett. 115 267210.
[13] Evans R F, Fan W J, Chureemart P, Ostler T A, Ellis M O A and Chantrell R W 2014 J. Phys. Condens. Matter 26, 103202.